Proximity-induced superconductivity within the insulating $(Li_{0.84}Fe_{0.16})OH$ layers in $(Li_{0.84}Fe_{0.16})OHFe_{0.98}Se$

Rustem Khasanov,[1,*] Huaxue Zhou,[2] Alex Amato,[1] Zurab Guguchia,[1] Elvezio Morenzoni,[1] Xiaoli Dong,[2] Guangming Zhang,[3] and Zhongxian Zhao[2]

[1]*Laboratory for Muon Spin Spectroscopy, Paul Scherrer Institut, CH-5232 Villigen PSI, Switzerland*

[2]*Beijing National Laboratory for Condensed Matter Physics, Institute of Physics & University of Chinese Academy of Science, CAS, Beijing 100190, China*

[3]*State Key Laboratory of Low-Dimensional Quantum Physics & Department of Physics, Tsinghua University, Beijing 100084, China*

(Received 19 February 2016; revised manuscript received 22 May 2016; published 15 June 2016)

The superconducting and magnetic properties of single crystalline $(Li_{0.84}Fe_{0.16})OHFe_{0.98}Se$ with the transition temperature $T_c \simeq 40$ K were studied by means of muon-spin rotation (μSR). The zero-field and field-shift μSR experiments confirm the homogeneity of the sample and the antiferromagnetic ordering within the $(Li_{0.84}Fe_{0.16})OH$ layers below $T_m \simeq 10$ K. The temperature dependence of the in-plane component of the magnetic penetration depth (λ_{ab}) was found to be consistent with gap opening within the superconducting FeSe planes, and it is well described within either the single s-wave gap or two s-wave gaps scenario. The opening of an additional small superconducting gap within the insulating $(Li_{1-x}Fe_x)OH$ layers was detected from the temperature evolution of the out-of plane component of the magnetic penetration $\lambda_c^{-2}(T)$. The superconductivity in $(Li_{0.84}Fe_{0.16})OH$ is most probably induced by the proximity to the superconducting FeSe layers.

DOI: 10.1103/PhysRevB.93.224512

I. INTRODUCTION

Recently, the iron chalcogenide system has attracted much interest due to a series of discoveries of new superconductors with high transition temperatures (T_c's). The superconducting transition temperature of $FeSe_{1-x}$ reaches values up to $T_c \simeq 37$ K by applying pressure [1]. An intercalation of the alkali metals (K, Cs, Rb) between FeSe layers increases T_c above 30 K [2–4]. The transition temperature value raises up to $T_c \simeq 100$ K in a single layer FeSe film grown on a $SrTiO_3$ substrate [5,6]. Significant enhancement of T_c is also observed in FeSe structures intercalated with alkali metal coordinated to molecular spacers (as, e.g., ammonia, pyridine, ethylenediamine, or hexamethylenediamine) [7–10] as well as by lithium-iron hydroxide [11–15]. In this case T_c was also claimed to increase with the increased two-dimensionality [16]. However, to date, the enhancement of two-dimensional properties caused by intercalation was solely related to the increased distance between the superconducting FeSe layers [10,16]. Due to the lack of good quality single crystals, the anisotropic physical properties as well as the role of the intermediate spacer layer were not yet studied. Recently Dong *et al.* [15] have reported the synthesis of high-quality single crystals of $(Li_{1-x}Fe_x)OHFeSe$ with T_c reaching $\simeq$42 K. The highly anisotropic properties of $(Li_{1-x}Fe_x)OHFeSe$ were confirmed in the measurements of the normal state resistivity and upper critical field.

In this paper we report on a detailed study of the evolution of the superconducting and magnetic properties of single crystalline $(Li_{0.84}Fe_{0.16})OHFe_{0.98}Se$ by using the muon-spin rotation (μSR) technique. The zero-field and field-shift μSR experiments confirm the homogeneity of the sample and the antiferromagnetic ordering within the $(Li_{0.84}Fe_{0.16})OH$ layers below $T_m \simeq 10$ K. The temperature dependence of the in-plane component of the magnetic penetration depth studied in transverse-field μSR experiment was found to be consistent with gap opening within the superconducting FeSe planes, and it is well described within either the single s-wave gap ($\Delta_s = 10.5$ meV) or two s-wave gaps ($\Delta_{s,1} = 15$ meV and $\Delta_{s,2} = 9$ meV) scenario in agreement with the results of ARPES [17] and STS [18] experiments, respectively. The opening of an additional small superconducting gap of unknown symmetry ($\simeq$1.05 meV and 1.5 meV in a case of s- and d-wave symmetry, respectively) was detected from the temperature evolution of the out-of plane component of the magnetic penetration $\lambda_c^{-2}(T)$. This gap, most probably, opens within the insulating $(Li_{1-x}Fe_x)OH$ layers and appears to be induced by the proximity to the superconducting FeSe layers. The strong enhancement of the out-of-plane superfluid density $\rho_{s,c} \propto \lambda_c^{-2}$ occurs at the same temperatures where the magnetism within the intermediate $(Li_{0.84}Fe_{0.16})OH$ layers sets in. The penetration depth anisotropy $\gamma = \lambda_c/\lambda_{ab}$ decreases from $\gamma \simeq 10$ at T_c to $\simeq 6$ at $T \simeq 1.6$ K.

The paper is organized as follows: In Sec. II we describe the sample preparation procedure and the application of the "surface muon" μSR technique to study thin single crystalline samples. The zero-field (ZF) and the transverse-field (TF) μSR data analysis procedure are described in Sec. III. Section IV A comprises studies of the magnetic response of the $(Li_{0.84}Fe_{0.16})OHFe_{0.98}Se$ sample. The field-shift experiments, the temperature dependencies of the in-plane and out of-plane components of the magnetic penetration depth are presented in Sec. IV B. The enhancement of two-dimensional properties and the interplay between the magnetism and superconductivity in $(Li_{1-x}Fe_x)OHFeSe$ system are briefly discussed in Secs. IV B 5 and IV C. The theoretical considerations of an interplay between the antiferromagnetically ordered and the superconducting layers are presented in Sec. IV C 1. The conclusions follow in Sec. V.

*rustem.khasanov@psi.ch

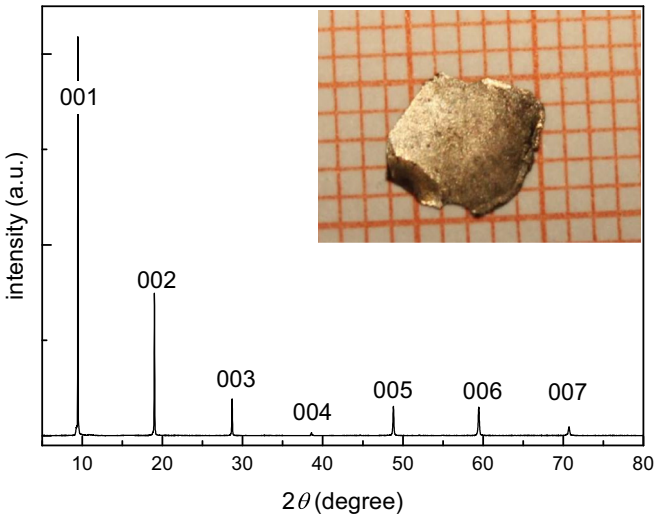

FIG. 1. The x-ray diffraction patterns of $(Li_{0.84}Fe_{0.16})OHFe_{0.98}Se$ single crystal demonstrating its orientations along (001) planes. The inset shows the photo of the single crystal used in our studies.

II. SAMPLE PREPARATION AND EXPERIMENTAL TECHNIQUES

A. Sample preparation

The superconducting $(Li_{0.84}Fe_{0.16})OHFe_{0.98}Se$ single crystal was synthesized by using the hydrothermal ion-exchange synthesis [15]. 0.012 mol selenourea (Alfa Aesar, 99.97% purity), 0.00375 mol Fe powder (Alfa Aesar, 99. 998% purity), 4 g $LiOHH_2O$ (Alfa Aesar, 99.996% purity), and one piece of nominal $K_{0.8}Fe_{1.6}Se_2$ precursor crystal were mixed with 5 ml deionized water. The mixture was loaded into the stainless steel autoclave and heated at 110 °C for 3 days. After that, the product, i.e., the $(Li_{0.84}Fe_{0.16})OHFe_{0.98}Se$ single crystal, was picked up and washed by deionized water several times. The photo of the $(Li_{0.84}Fe_{0.16})OHFe_{0.98}Se$ single crystal used in the present study is shown in the inset of Fig. 1. The crystal dimensions are $\simeq 5.6 \times 4.6 \times 0.125$ mm^3.

B. Experimental techniques

X-ray diffraction (XRD) measurements were carried out at a room temperature on a Rigaku Ultima IV (3KW) diffractometer using Cu-K_α radiation. The room temperature x-ray diffraction (XRD) patterns demonstrate a good sample quality and its orientation along (001) planes (see Fig. 1).

The magnetic measurements were conducted on a Quantum Design MPMS-XL1 system with a remanent field lower than 0.4 μT. The zero-field cooled (ZFC) and field cooled (FC) magnetization curves measured at $\mu_0 H = 0.1$ mT applied along the ab plane are shown in Fig. 2(a). A sharp diamagnetic transition occurs at about 40.5 K. The ZFC magnetization curve measured at $\mu_0 H = 10$ mT is shown in Fig. 2(b). Note the absence of "ferromagneticlike" features as observed by Pachmayr *et al.* [12] on $[(Li_{1-x}Fe_x)OH](Fe_{1-y}Li_y)Se$.

The muon spin rotation (μSR) experiments were carried out at the πM3 beam line at the Paul Scherrer Institute, Switzerland. The zero-field (ZF) and transverse-field (TF) μSR measurements were performed at temperatures ranging from $\simeq$1.5 to 50 K. In TF measurements the external magnetic field was applied perpendicular to the muon-spin polarization. The typical counting statistics were $\sim 15 - 20 \times 10^6$ positron events for each data point.

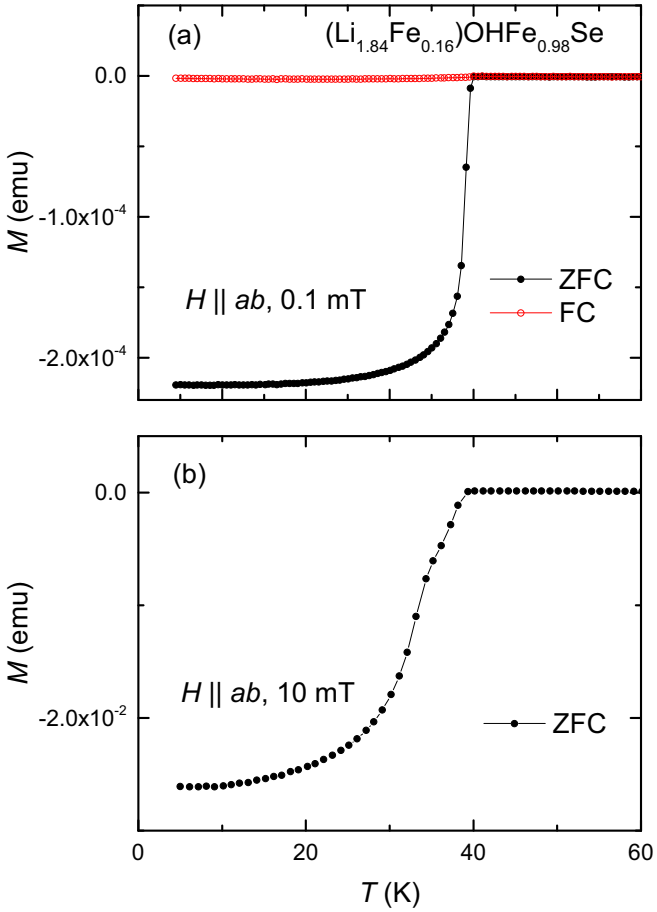

FIG. 2. (a) The zero-field cooled (ZFC) and field cooled (FC) magnetization curves measured at $\mu_0 H = 0.1$ mT applied along the ab plane. (b) ZFC magnetization curve measured at $\mu_0 H = 10$ mT. Note the absence of "ferromagneticlike" features as observed by Pachmayr *et al.* [12] on $[(Li_{1-x}Fe_x)OH](Fe_{1-y}Li_y)Se$.

C. Application of the "surface muon" μSR technique to study thin samples

So called "surface" muons with momentum of $\simeq$28.6 MeV/c and kinetic energy of $\simeq$4.1 MeV (as used in our studies) stop in the matter at the depth of about 0.15 g/cm^2. For $(Li_{0.84}Fe_{0.16})OHFe_{0.98}Se$ with the density of $\simeq$4 g/cm^3 this corresponds to a depth of $\simeq$0.4 mm. In order to measure the sample with a thickness of $\simeq$0.1 mm, as $(Li_{0.84}Fe_{0.16})OHFe_{0.98}Se$ single crystal studied here, a special sample holder was constructed. The schematic view of the experimental setup is presented in Fig. 3. The sample was sandwiched between two pieces made of several 0.125 mm thick Kapton sheets. The first few Kapton layers play a role of a "degrader" by decelerating the muons in the incoming muon beam. After passing the degrader the muons are already slow enough to be stopped in the sample. The last layers are used to stop the muons which were still able to go through the sample.

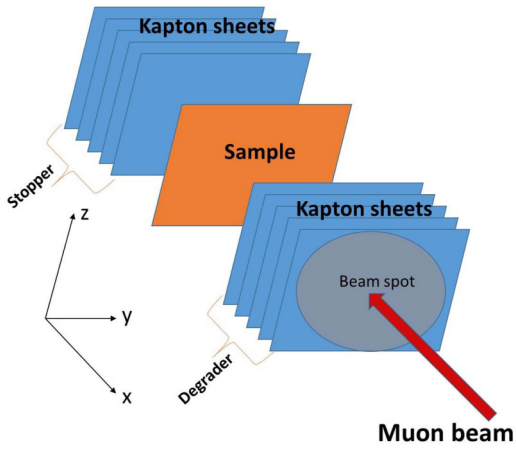

FIG. 3. The schematic view of the experimental setup for μSR experiments on thin single-crystalline samples. The first few Kapton layers play a role of degrader by decelerating the muons in the incoming muon beam. The last layers are used in order to stop the muons passing the sample. The crystallographic c axis of the $(Li_{0.84}Fe_{0.16})OHFe_{0.98}Se$ is aligned along the x direction.

The reliable thickness of the "degrader" layer (5×0.125 mm Kapton sheets) as well as the ZF- and TF-μSR response of Kapton were determined in the separate set of experiments.

III. ZF- AND TF-μSR DATA ANALYSIS PROCEDURE

A. ZF-μSR data analysis procedure

The μSR experiments in zero field (ZF-μSR) were performed in order to study the magnetic response of the sample. In two sets of experiments the initial muon-spin polarization $P(0)$ was applied parallel to the crystallographic c axis and the ab plane, respectively. For the experimental setup presented in Fig. 3 it corresponds to cases with $P(0) \parallel x$ and $P(0) \parallel z$ directions, correspondingly. A few representative muon-time spectra for both initial muon-spin orientations are shown in Fig. 4.

The asymmetry $A(t)$ in the whole temperature range and for both orientations was fitted by using the following functional form:

$$\frac{A_{ZF}(t)}{A_{ZF}(0)} = f_m\,[f_p\,e^{-\Lambda_T t} + (1-f_p)\,e^{-\Lambda_L t}] + (1-f_m)\,e^{-\Lambda t}\mathrm{GKT}(t) + BG. \quad (1)$$

The first and the second terms on the right hand site represent contributions from the magnetically ordered parts of the sample and those remaining in the nonmagnetic state. f_m is the magnetic fraction with the corresponding transversal (Λ_T) and longitudinal (Λ_L) relaxation rates; f_p is the fraction of muons experiencing precession in the internal fields (in powder samples $f_p \equiv 2/3$); GKT is the Gaussian Kubo-Toyabe relaxation function representing the contribution of nuclear moments; Λ represents the relaxation caused by randomly distributed magnetic impurities; and BG is the background contribution caused by muons missing the sample and/or stopped in Kapton layers.

Both data sets [$P(0) \parallel c$ and $P(0) \parallel ab$] were fitted simultaneously (all runs within the single fit procedure). For each particular temperature the parameters f_m, Λ_L, Λ_T, and Λ were assumed to be the same for $P(0) \parallel c$ and $P(0) \parallel ab$ set of measurements. f_p and the Gaussian Kubo-Toyabe relaxation σ_{GKT} entering GKT function were assumed to be dependent on the orientation and independent on temperature.

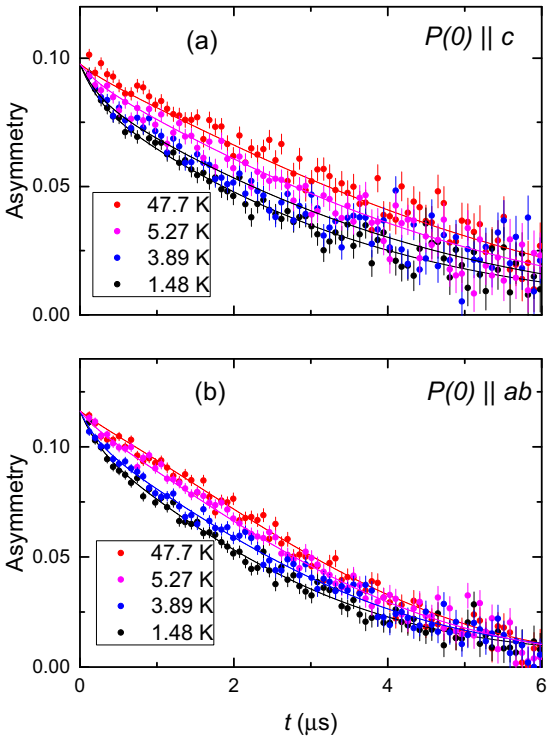

FIG. 4. The zero-field muon-time spectra measured with the initial muon-spin polarization $P(0)$ applied parallel to the crystallographic c axis (a) and the ab plane (b).

B. TF-μSR data analysis procedure

Two sets of field-cooled TF-μSR experiments with the magnetic field (H) applied parallel to the c axis and the ab plane were performed. Following the experimental setup presented in Fig. 3 the first ($H \parallel c$) case corresponds to the magnetic field and the initial muon-spin polarization [$P(0)$] applied along the x and z direction, correspondingly. In the second set of experiments ($H \parallel ab$), the orientation of $P(0)$ was kept the same, while the magnetic field was applied along the y axes.

Figure 5 shows the TF-μSR time spectra measured with the external field $\mu_0 H = 12$ mT applied parallel to the crystallographic c direction above ($T = 42.4$ K) and below ($T = 1.5$ K) the superconducting transition temperature T_c. The stronger damping at $T \simeq 1.5$ K is caused by the nonuniform field distribution in the flux-line lattice.

In order to account for the asymmetric field distribution $P(B)$ in the superconductor in the vortex state (see, e.g., Ref. [19] and Sec. IV B 1) the $H \parallel c$ data were analyzed by using the skewed Gaussian (SKG) field distribution [20]:

$$P_{\mathrm{skg}}(B) = \sqrt{\frac{2}{\pi}}\frac{\gamma_\mu}{\sigma_+ + \sigma_-}\begin{cases}\exp\left[-\frac{1}{2}\frac{(B-B_0)^2}{(\sigma_+/\gamma_\mu)^2}\right] & B \geqslant B_0 \\ \exp\left[-\frac{1}{2}\frac{(B-B_0)^2}{(\sigma_-/\gamma_\mu)^2}\right] & B < B_0\end{cases}. \quad (2)$$

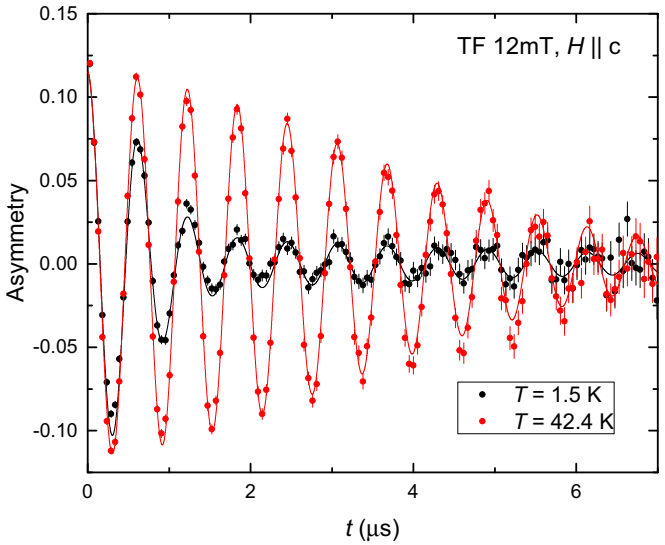

FIG. 5. TF-μSR time-spectra of $(La_{0.84}Fe_{0.16})OHFe_{0.98}Se$ measured in $H \parallel c$ direction ($\mu_0 H = 12$ mT) below ($T = 1.5$ K) and above ($T = 42.4$ K) the superconducting transition temperature. The stronger damping in the superconducting state is due to the formation of the vortex lattice.

Here $\gamma_\mu = 2\pi 135.5$ MHz/T is the muon gyromagnetic ratio; B_0 is the field corresponding to the maximum of $P(B)$ distribution; σ_+ and σ_- are Gaussian widths of the distribution above and below B_0, respectively.

The first (M_1) and the second (M_2) moments of the SKG distribution are [20]:

$$M_1 = \langle B \rangle = B_0 + \sqrt{\frac{2}{\pi}} \frac{\sigma_+ - \sigma_-}{\gamma_\mu} \tag{3}$$

and

$$M_2 = \frac{1}{\pi \gamma_\mu^2} \left[(\pi - 2)\, \sigma_-^2 - (\pi - 4)\, \sigma_+ \sigma_- + (\pi - 2)\, \sigma_+^2 \right]. \tag{4}$$

In order to fit the SKG distribution to the experimental TF-μSR data the transformation from the field domain to the time domain is performed via [20]:

$$\mathrm{SKG}(t) = \int_{-\infty}^{\infty} P_{\mathrm{skg}}(B)\, \cos(\gamma_\mu B t)\, dB. \tag{5}$$

Finally, by considering the magnetic response of $(Li_{0.84}Fe_{0.16})OHFe_{0.98}Se$ studied in the ZF-μSR experiment (see Sec. IV A), the TF-μSR data for $H \parallel c$ orientation were fitted as:

$$\frac{A_{TF}(t)}{A_{TF}(0)} = (1 - f_m)\, \mathrm{SKG}(t) \times e^{-\Lambda_{TF} t} + BG. \tag{6}$$

Here Λ_{TF} is the exponential relaxation caused by magnetic impurities. Following Ref. [21], Λ_{TF} relates to the value measured in the zero field (see Sec. IV A) as $\Lambda_{TF} \simeq 0.56\, \Lambda$. The prefactor $(1 - f_m)$ accounts for the fraction of muons experiencing oscillations in parts of the sample remaining nonmagnetic (see Sec. IV A). For the analysis of the TF spectra the BG term includes the magnetic contribution.

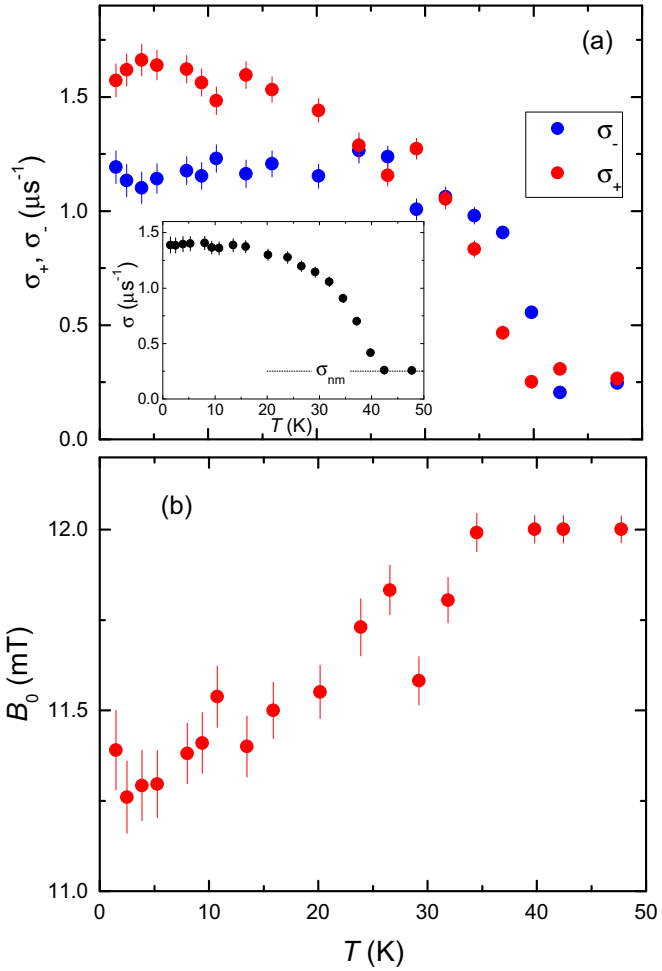

FIG. 6. Temperature dependences of σ_+ and σ_- (panel a) and B_0 (panel b) obtained from the fit of TF-μSR data by using Eq. (6). The external field $\mu_0 H = 12$ mT is applied parallel to the crystallographic c axis. The inset in panel a shows the square root of the second moment σ as calculated by using Eq. (4). σ_{nm} is the nuclear moment contribution measured above T_c.

The results of the analysis are presented in Fig. 6. The inset in Fig. 6(a) shows the temperature dependence of the square root of the second moment $\sigma = (M_2)^{1/2}$ obtained by using Eq. (4).

The second set of TF-μSR experiments was performed by applying the external field ($\mu_0 H = 10.8$ mT) parallel to the ab plane. The analysis reveals that within the whole temperature range the field distribution $P(B)$ remains symmetric and could be well described by single Gaussian distribution function. In analogy with the $H \parallel c$ case, described above, the $H \parallel ab$ set of data was fitted by using the following functional form:

$$\frac{A_{TF}(t)}{A_{TF}(0)} = (1 - f_m)\, e^{-\sigma^2 t^2/2} \times e^{-\Lambda_{TF} t} \cos(\gamma_\mu B t + \phi) + BG. \tag{7}$$

The meaning of the parameters are the same as in Eq. (6). ϕ is the initial phase of the muon-spin ensemble. Note that the Gaussian distribution function is the trivial case of SKG one

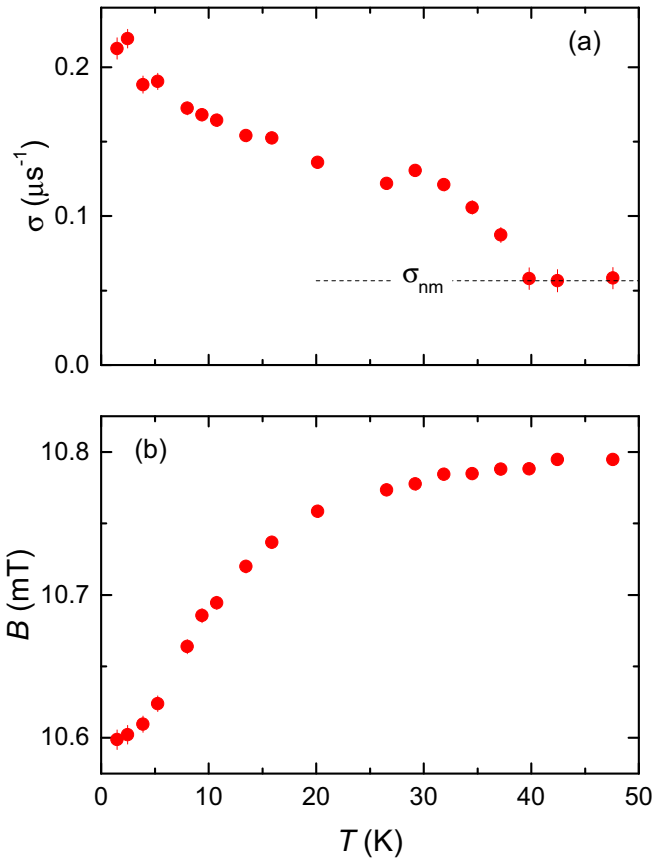

FIG. 7. Temperature dependences of the Gaussian relaxation rate σ (panel a) and the internal field B (panel b) obtained from the fit of TF-μSR data by using Eq. (7). The external field $\mu_0 H = 10.8$ mT is applied parallel to the ab plane. σ_{nm} is the nuclear moment contribution measured above T_c.

with $\sigma = \sigma_+ = \sigma_-$. The results of the analysis of $H \parallel ab$ data are presented in Fig. 7.

C. Determination of the in-plane and the out-of-plane components of the magnetic penetration depth

The superconducting contribution to the square root of the second moment σ was further calculated by subtracting the nuclear dipolar contribution measured above T_c [σ_{nm}, see the inset in Figs. 6(a) and 7(a)] as:

$$\sigma_{sc}^2 = \sigma^2 - \sigma_{nm}^2. \tag{8}$$

In extreme type II superconductor σ_{sc} is related to the magnetic penetration depth λ by the expression [22]:

$$\frac{\sigma_{sc}^2}{\gamma_\mu^2} = 0.00371 \frac{\Phi_0^2}{\lambda^4(T)} \tag{9}$$

($\Phi_0 = 2.068 \times 10^{-15}$ Wb is the magnetic flux quantum).

According to the London model, the inverse squared magnetic field penetration depth for the isotropic superconductor is proportional to the so-called superfluid density in terms of $\lambda^{-2} \propto \rho_s = n_s/m^*$ (ρ_s is the superfluid density, n_s is the charge carrier concentration, and m^* is the effective mass of the charge carriers). For an anisotropic superconductor the magnetic penetration depth is also anisotropic and is determined by an effective mass tensor [23]:

$$m_{\text{eff}} = \begin{pmatrix} m_i^* & 0 & 0 \\ 0 & m_j^* & 0 \\ 0 & 0 & m_k^* \end{pmatrix}, \tag{10}$$

where m_i^* is the mass of the carrier flowing along the ith principal axis. The effective penetration depth for the magnetic field applied along the ith principal axis of the effective mass tensor is then given as [23]:

$$\lambda_{jk}^{-2} = \frac{1}{\lambda_j \lambda_k} \propto \sigma^{\parallel i}. \tag{11}$$

For convenience we drop index "sc" in the superconducting part of the square root of the second moment σ_{sc}. Equation (11) implies that by applying the magnetic field along the crystallographic a, b, and c directions one measures $\sigma^{\parallel a} \propto 1/\lambda_b \lambda_c$, $\sigma^{\parallel b} \propto 1/\lambda_a \lambda_c$, and $\sigma^{\parallel c} \propto 1/\lambda_a \lambda_b$, respectively.

For the particular $(La_{0.84}Fe_{0.16})OHFe_{0.98}Se$ sample studied here, $\lambda_a = \lambda_b$, so by applying the magnetic field along principal c direction the in-plane component of the magnetic penetration depth (λ_{ab}) is obtained:

$$\lambda_{ab}^{-2}\ (\mu\text{m}^{-2}) = 9.32(\mu\text{m}^{-2}/\mu\text{s}^{-1}) \times \sigma^{\parallel c}\ (\mu\text{s}^{-1}). \tag{12}$$

The out-of-plane component of the magnetic penetration depth (λ_c) can be calculated by combining the results of $H \parallel c$ and $H \parallel ab$ experiments as:

$$\lambda_c^{-2}\ (\mu\text{m}^{-2}) = 9.32(\mu\text{m}^{-2}/\mu\text{s}^{-1}) \times \frac{(\sigma^{\parallel ab})^2\ (\mu\text{s}^{-2})}{\sigma^{\parallel c}\ (\mu\text{s}^{-1})}. \tag{13}$$

IV. RESULTS AND DISCUSSIONS

A. Magnetism of $(Li_{0.84}Fe_{0.16})OHFe_{0.98}Se$

Dependencies of the magnetic volume fraction f_m and the exponential relaxation rate Λ on temperature measured in ZF-μSR experiments are presented in Figs. 8(a) and 8(b). Both dependencies were obtained from the simultaneous (global) fit of $P(0) \parallel c$ and $P(0) \parallel ab$ sets of data by using Eq. (1) (see Sec. III A). Figure 8(a) implies that the magnetic fraction f_m is nearly zero down to ~10–15 K and increases up to $\simeq$20% with the temperature decrease down to $T \simeq 1.5$ K. A similar tendency is observed for the exponential relaxation rate Λ which stays almost constant down to $\simeq$10 K and increases from $\simeq 0.15\ \mu\text{s}^{-1}$ to $0.25\ \mu\text{s}^{-1}$ with the temperature decrease down to $\simeq$1.5 K [see Fig. 8(b)].

From the data presented in Figs. 8(a) and 8(b) two important points emerge. (i) Following Refs. [11,12,24] the intermediate $(Li_{1-x}Fe_x)OH$ layer becomes fully magnetic at low temperatures. Since in our experiments up to 80% of all the muons are not sensitive to the bulk magnetic order, we may suggest the presence of two stopping sites where the muons come to the rest. Following calculations of Bendele *et al.* [25] for superconducting $FeSe_{1-x}$ system, the first (nonmagnetic) site corresponds to muons stopped between Fe atoms within the FeSe layer. It is located on the line connecting the Se-Se ions along the c direction and has the same $4g$ local point symmetry as Se ions [25]. The second site corresponds to muons stopped within the $(Li_{0.84}Fe_{0.16})OH$ layer, which orders magnetically below 10 K. (ii) The magnetic order within the $(Li_{0.84}Fe_{0.16})OH$ layer influences spins of muons stopped

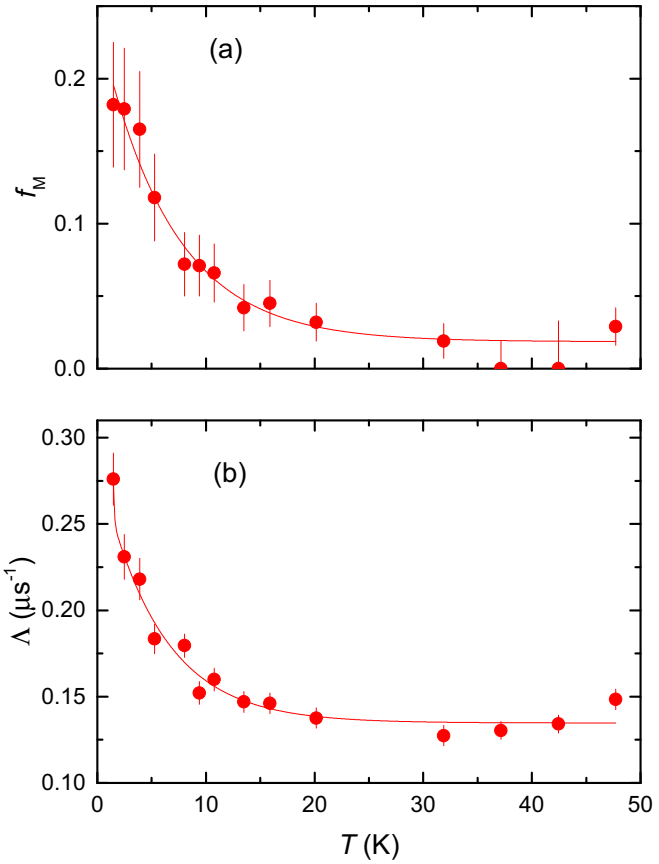

FIG. 8. (a) Temperature dependence of the magnetic volume fraction f_m of $(Li_{0.84}Fe_{0.16})OHFe_{0.98}Se$ as observed by means of ZF-μSR. (b) Temperature dependence of the exponential relaxation rate Λ. Lines in (a) and (b) are guides to the eye.

within the nonmagnetic FeSe layer. Indeed, for $T \lesssim 10$ K the exponential relaxation rate Λ increases almost in the same way as the magnetic fraction f_m.

B. Superconductivity of $(Li_{0.84}Fe_{0.16})OHFe_{0.98}Se$

1. *The homogeneity of the superconducting state: Field-shift experiments*

The homogeneity of the superconducting state was checked by performing a series of field-shift experiments in transverse-field (TF) configuration. Figure 9 exhibits the fast Fourier transform of the TF-μSR time spectra, which reflects the internal field distribution $P(B)$. The black symbols correspond to $P(B)$ obtained after cooling the sample at $\mu_0 H = 12$ mT ($H \parallel c$) from a temperature above T_c down to 1.48 K [Fig. 9(a)] and 20.2 K [Fig. 9(b)]. The red symbols are $P(B)$ distributions after field cooling in 12 mT and subsequently increasing it up to 15 mT. The solid black and red lines represent the corresponding fits of Eq. (6) to the data. The analysis reveal that the main part of the signal, accounting for approximately 92% of the total signal amplitude, remains unchanged within the experimental error. Only the sharp peak ($\simeq$8% of the signal amplitude) follows exactly the applied field. It is attributed, therefore, to the residual background signal from muons missing the sample (see also Ref. [26] where the

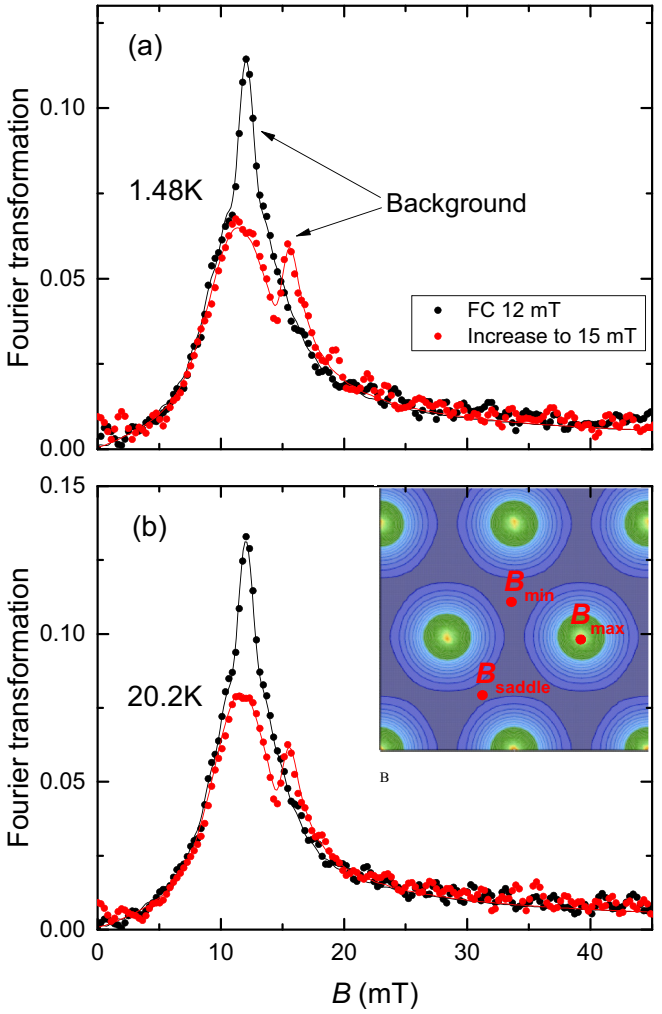

FIG. 9. Fast Fourier transform of TF-μSR time spectra after cooling in an applied field of $\mu_0 H = 12$ mT, $H \parallel c$, (black symbols) and after a subsequent field increase to 15 mT (red symbols) at $T = 1.48$ K (a) and 20.2 K (b). The solid lines are fits by using Eq. (6). The inset in (b) is the contour plot of the field variation within the triangular vortex lattice. B_{min}, B_{max}, and B_{saddle} are the minimum, maximum, and the saddle point fields.

μSR field-shift experiments were introduced). The field-shift experiment clearly demonstrates that the vortex lattice in $(Li_{0.84}Fe_{0.16})OHFe_{0.98}Se$ sample is strongly pinned in a similar way above (20.2 K) and below (1.48 K) the magnetic ordering temperature ($T_m \simeq 10$ K).

The asymmetric $P(B)$ distributions reported in Fig. 9 possess the basic features expected for a well aligned vortex lattice. In the case of triangular lattice [inset in Fig. 9(b)] the cutoff at low fields corresponds to the minimum in $P(B)$ occurring at the midpoint of three adjacent vortices (B_{min}). The peak arises from the saddle point midway between two adjacent vortices (B_{saddle}), whereas the long tail towards high fields is due to the region around the vortex core (B_{max}).

2. *Temperature dependence of* λ_{ab}^{-2}

The temperature dependence of the inverse squared in-plane magnetic penetration depth $\lambda_{ab}^{-2} \propto \rho_{s,ab}$ is shown in Fig. 10(a).

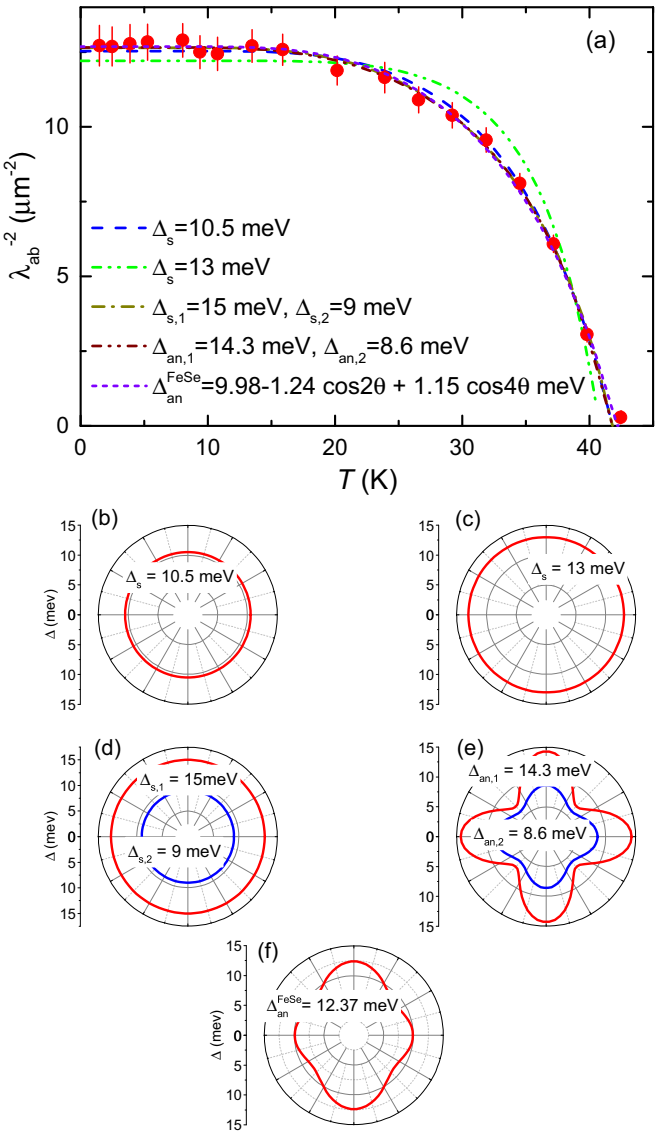

FIG. 10. (a) Temperature dependence of λ_{ab}^{-2} of $(Li_{0.84}Fe_{0.16})OHFe_{0.98}Se$. The fitting curves were obtained within the following models of gap symmetries: s wave: $\Delta_s = 10.5$ meV (Ref. [17] and panel b); s wave: $\Delta_s = 13$ meV (Ref. [27] and panel c); two s-wave gaps: $\Delta_{s,1} = 15$ meV and $\Delta_{s,2} = 9$ meV (Ref. [18] and panel d); two anisotropic gaps: $\Delta_{an,1} = 14.3$ meV $\cdot [1 - 0.25(1 - \cos 4\varphi)] \Delta_{an,2} = 8.6$ meV $\cdot [1 - 0.15(1 - \cos 4\varphi)]$ (Ref. [28] and panel e) and the anisotropic gap in the single-layer FeSe on the $SrTiO_3$ substrate: $\Delta_{an}^{FeSe} = 9.98 - 1.24\cos 2\theta + 1.15\cos 4\theta$ meV (Ref. [32] and panel f).

Note that the temperature dependence of λ_{ab}^{-2} is primarily determined by the superconducting gap(s) opening in the ab plane. They should correspond to the ones measured directly in recent angle-resolved photoemission (ARPES) and scanning tunneling spectroscopy (STS) experiments [17,18,27,28]. At present, there is no consistency on the number of gaps (one versus two), their symmetries, and absolute values. ARPES experiments reveal the presence of a single band around the M point at the Brillouin zone with an isotropic (s-wave) gap. The reported gap value varies between $\Delta_s = 10.5$ meV and $\simeq$13 meV [17,27]. STS experiments point to the presence of two sets of electron pockets near the M point with different symmetries and high values of the gaps. Two s-wave gaps with $\Delta_{s,1} \simeq 15$ meV and $\Delta_{s,2} \simeq 9$ meV were found in Ref. [18], while two anisotropic gaps with maximum values $\Delta_{an,1} = 14.3$ meV and $\Delta_{an,2} = 8.6$ meV were observed in Ref. [28]. The angular distributions of gaps reported in Refs. [17,18,27,28] are shown schematically in Figs. 10(b)–10(e).

The temperature dependence of λ_{ab}^{-2} was further analyzed within the local (London) approach by using the following functional form [29,30]:

$$\frac{\lambda^{-2}(T)}{\lambda^{-2}(0)} = 1 + \frac{1}{\pi}\int_0^{2\pi}\int_{\Delta(T,\varphi)}^{\infty}\left(\frac{\partial f}{\partial E}\right)\frac{E\,dE d\varphi}{\sqrt{E^2 - \Delta(T,\varphi)^2}}. \quad (14)$$

Here $\lambda^{-2}(0)$ is the zero-temperature value of the magnetic penetration depth, $f = [1 + \exp(E/k_BT)]^{-1}$ is the Fermi function, φ is the angle along the Fermi surface, and $\Delta(T,\varphi) = \Delta\, g(\varphi) \tanh\{1.82[1.018(T_c/T - 1)]^{0.51}\}$ [Δ is the gap value at $T = 0$] [30]. $g(\varphi)$ describes the angular dependence of the gap: $g_s(\varphi) = 1$ for the s-wave gap, $g_{an}(\varphi) = [1 - a(1 - \cos 4\varphi)]$ for the anisotropic gap [28], and $g_d(\varphi) = |\cos(2\varphi)|$ for the d-wave gap.

The two-gap analysis was performed within the framework of the phenomenological α model [30,31]:

$$\frac{\lambda^{-2}(T)}{\lambda^{-2}(0)} = \omega\,\frac{\lambda^{-2}(T,\Delta_1)}{\lambda^{-2}(0,\Delta_1)} + (1 - \omega)\,\frac{\lambda^{-2}(T,\Delta_2)}{\lambda^{-2}(0,\Delta_2)}. \quad (15)$$

Here ω $(0 \leqslant \omega \leqslant 1)$ is the weight factor representing the relative contribution of the larger gap to λ^{-2}.

The results of the analysis are presented in Fig. 10(a) and Table I. It should be noted here that the fits were performed by using the gap values and the gap symmetries as measured in ARPES and STS experiments (see Refs. [17,18,27,28] and also Figs. 10(b)–10(e)). The only free parameters were $\lambda_{ab}^2(0)$ and T_c in the case of single s-wave gap fits and $\lambda_{ab}^2(0)$, T_c, and ω within a two-gap approach. Obviously, three out of four gap models describe the obtained $\lambda_{ab}^{-2}(T)$ dependence almost equally well. Only the curve with $\Delta_s = 13$ meV deviates significantly from the data.

Two important points need to be considered: (i) The analysis reveals that within the single s-wave gap approach a satisfactory agreement between the fit and the data is achieved for $9.8 \lesssim \Delta_s \lesssim 10.6$ meV. The gap value of 10.5 meV measured in Ref. [17] stays within this limit, while the value of 13 meV from Ref. [27] is $\simeq$15% higher. (ii) As shown in Table I, in the case of two anisotropic gaps, the relative weight of the smaller gap is consistent with zero. This suggests that the bands where the smaller gap is supposed to open do not supply *any* supercarriers to the superfluid density and, consequently, the energy gap cannot exist. However, the analysis reveals that by decreasing the degree of the larger gap anisotropy ($a = 0.25$, Ref. [28]), the weight of the smaller gap continuously increases, reaching $\simeq$40% for $a = 0$. This implies that if the two anisotropic gaps scenario is realized in $(Li_{1-x}Fe_x)OHFeSe$, the larger gap should have a smaller anisotropy than suggested in Ref. [28].

TABLE I. Summary of the in-plane (λ_{ab}) and the out-of-plane (λ_c) magnetic penetration depth studies of $(Li_{0.84}Fe_{0.16})OHFe_{0.98}Se$. The analysis of λ_{ab}^{-2} was performed by using the gap values and the gap symmetries as reported in Refs. [17,18,27,28]. In the analysis of λ_c^{-2}, the large gap and T_c were fixed to $\Delta_s = 10.5$ meV and $T_c = 41.9$ K, respectively. The respective meaning of the parameters is: T_c: transition temperature; $\lambda(0)^{-2}$: zero-temperature value of inverse squared magnetic penetration depth; and ω is the relative weight of the larger gap to λ^{-2}.

	Model	Gap Value(s) (meV)	Reference	T_c (K)	$\lambda^{-2}(0)$ (μm^{-2})	ω
	s-wave gap	10.5	[17]	41.9(1)	12.54(4)	
	s-wave gap	13	[27]	40.8(1)	12.21(6)	
λ_{ab}^{-2}	$s+s$-wave gaps	15/9	[18]	41.9(1)	12.65(3)	0.27(3)
	$an+an$ gaps	14.3/8.6	[28]	41.7(1)	12.65(3)	1.00(2)
	$s+s$-wave gaps	10.5/1.05(3)		41.9	0.298(6)	0.39(3)
λ_c^{-2}	$s+d$-wave gap	10.5/1.50(3)		41.9	0.326(6)	0.34(3)

3. *Consistency of the in-plane superfluid density with the anisotropic gap of the single-layer FeSe on the* $SrTiO_3$ *substrate*

The similarity in electronic behavior of $(Li_{1-x}Fe_x)OHFeSe$ and the single-layer FeSe on the $SrTiO_3$ substrate could be further confirmed by comparing the consistency of the in-plane superfluid density $\rho_{s,ab} \propto \lambda_{ab}^{-2}$ with the most precise gap measurement performed recently by Zhang *et al.* [32] by means of ARPES. Following Ref. [32] the gap in the single-layer FeSe on the $SrTiO_3$ substrate is anisotropic and is described as:

$$\Delta(\varphi) = 9.98 - 1.24\ \cos 2\theta + 1.15\ \cos 4\theta \text{ meV}. \quad (16)$$

The results of the fit with the gap described by the above equation is shown in Fig. 10(a). The angular dependence of the gap is presented in the panel f. During the fit $\lambda_{ab}^{-2}(0)$ and T_c were kept free and were found to be 12.67(3) μs^{-2} and 42.2(1) K, respectively.

4. *Temperature dependence of* λ_c^{-2}

The temperature dependence of the inverse squared out-of-plane magnetic penetration depth $\lambda_c^{-2} \propto \rho_{s,c}$ is shown in Fig. 11. It is reasonable to assume that the superconducting energy gap(s) detected within the ab plane should remain the same in the perpendicular direction. This seems to be correct for some Fe-based superconductors as, e.g., $SrFe_{1.75}Co_{0.25}As_2$ [33], $FeSe_{0.5}Te_{0.5}$ [34], LiFeAs [35], which are characterized by relatively small values of the anisotropy parameter $\gamma_\lambda = \lambda_c/\lambda_{ab}$. By lowering the temperature γ_λ changes from $\gamma_\lambda \simeq 2.0$, 1.5, and 2.0 close to T_c to $\gamma_\lambda \simeq 2.7$, 2.5, and 1.0 at $T \simeq 0$ for $SrFe_{1.75}Co_{0.25}As_2$, $FeSe_{0.5}Te_{0.5}$ and LiFeAs, respectively [33–35].

The analysis reveals, however, that *none* of the gap models describing $\lambda_{ab}^{-2}(T)$ agree with the $\lambda_c^{-2}(T)$ dependence. The inflection point at $T \simeq 10$ K clearly implies that a superconducting gap with an absolute value much smaller than determined by means of ARPES and STS is present. Bearing this in mind and accounting for the simplest s-wave model describing $\lambda_{ab}^{-2}(T)$ ($\Delta_s = 10.5$ meV, $T_c = 41.9$ K, see Fig. 10 and Table I), the two-gap model (Eq. (15)) with the larger gap $\Delta_s = 10.5$ meV and the smaller gap remaining as a free parameter was fitted to the $\lambda_c^{-2}(T)$. For the smaller gap the s-wave and d-wave type of symmetries were considered. The results of the fit are presented in Fig. 11(a) and Table I. The angular distributions of the gaps in the case of $s+s$ and $s+d$ model fittings are shown schematically in Figs. 11(b) and 11(c). Both $s+s$ and $s+d$ gap models fit $\lambda_c^{-2}(T)$ equally well. One cannot distinguish between them within the accuracy of the experiment. The gap values ($\Delta_{s,2} = 1.05$ meV and $\Delta_d = 1.50$ meV) are a factor of 5 to 10 lower than the smallest gap within the ab plane. This clearly differentiates $(Li_{1-x}Fe_x)OHFeSe$ from other Fe-based superconductors where the gap(s) were found to be essentially direction independent.

5. *Enhanced two-dimensional properties of* $(Li_{1-x}Fe_x)OHFeSe$

In $(Li_{1-x}Fe_x)OHFeSe$ the FeSe layers are weakly bonded to the intermediate $(Li_{1-x}Fe_x)OH$ layers via hydrogen atoms.

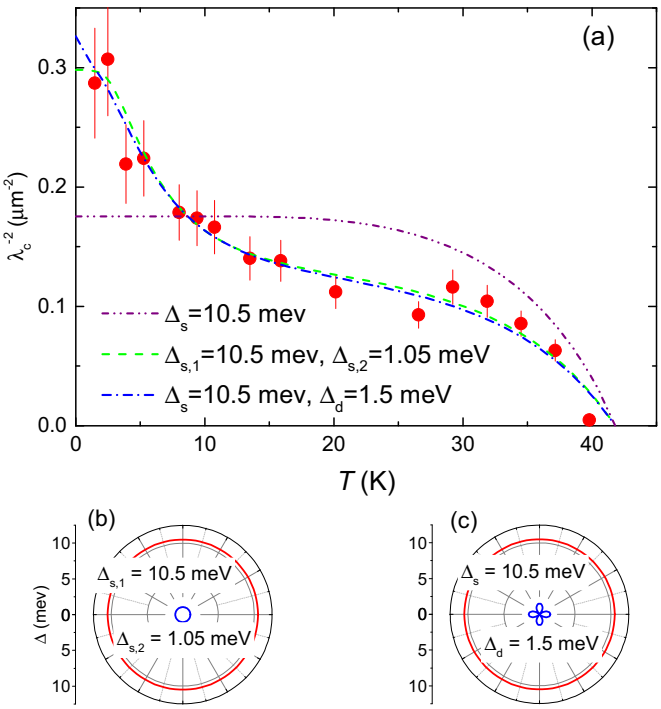

FIG. 11. (a) Temperature dependence of λ_c^{-2} of $(Li_{0.84}Fe_{0.16})OHFe_{0.98}Se$. The fitting curves were obtained within the $s+s$ (b) and $s+d$ (c) gap symmetries. The larger gap and T_c were fixed to $\Delta_s = 10.5$ meV and $T_c = 41.9$ K, respectively. The curve with $\Delta_s = 10.5$ meV is shown for comparison with $\lambda_{ab}^{-2}(T)$ data (see Fig. 10).

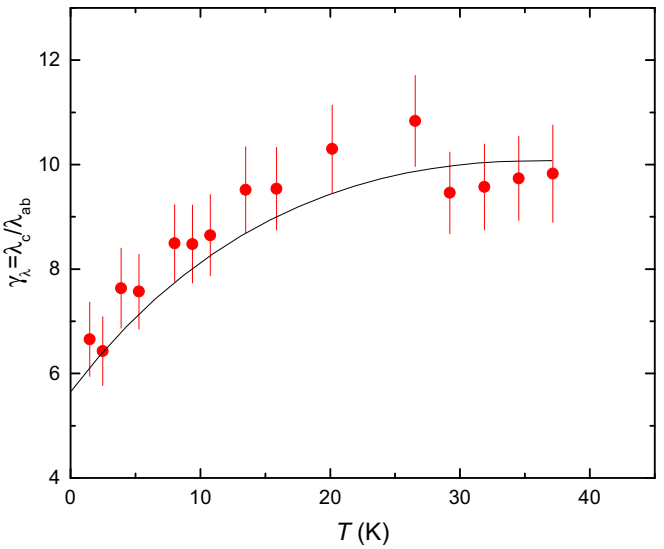

FIG. 12. The temperature dependence of the anisotropy parameter $\gamma_\lambda = \lambda_c/\lambda_{ab}$. The line is a guide for the eye.

The distance between the superconducting FeSe layers ($\simeq$9.3 Å) is also higher than in most of the Fe-based superconducting families (including, e.g., 11, 111, 122, and 245 families). This clearly indicates that $(Li_{1-x}Fe_x)$OHFeSe has a highly two-dimensional character, which is also confirmed experimentally by: (i) the observation of an extremely high resistivity ratio ρ_c/ρ_{ab} which increases continuously with decreasing temperature by reaching the value of $\rho_c/\rho_{ab} \simeq 2500$ at $T = 50$ K [15]. (ii) The similar electronic structure of $(Li_{1-x}Fe_x)$OHFeSe and the single-layer FeSe on the $SrTiO_3$ substrate observed by means of ARPES and STS [17,18,27,28]. Both systems were found to have a similar Fermi-surface topology, band structure, and superconducting gap symmetry. This statement is further confirmed by an agreement of our $\lambda_{ab}^{-2}(T)$ data with the recent gap measurements from Ref. [32] (see Sec. IV B 3); (iii) The present observation of a high value of the magnetic field penetration depth anisotropy. $\gamma_\lambda = \lambda_c/\lambda_{ab} \simeq 10$ close to T_c which decreases to $\simeq$7 at $T = 1.5$ K (see Fig. 12).

We believe therefore that the enhanced two-dimensionality of $(Li_{1-x}Fe_x)$OHFeSe leads to the unusual observation of a smaller gap opening along the crystallographic c direction. The large s-wave gap(s) (or large anisotropic gaps, see Table I) correspond to a condensation of the supercarriers confined within the two-dimensional FeSe layers, whereas the tiny small gap opens in the $(Li_{1-x}Fe_x)$OH layers and is induced by the superconducting FeSe layers due to proximity effects. Such a situation is similar to the appearance of a proximity-induced gap in CuO chains in the cuprate superconductor $YBa_2Cu_4O_8$ [36]. The superconducting gap detected in the chains ($\simeq$5 meV) is significantly smaller than the gap in the superconducting CuO_2 planes ($\simeq$20 meV) [37] and is confined within a very narrow k-space region. We should stress, however, on the significant difference between $(Li_{1-x}Fe_x)$OHFeSe studied here and $YBa_2Cu_4O_8$. In the later compound the chains are metallic and, therefore, allow for conductivity (superconductivity) along the chain direction. In $(Li_{1-x}Fe_x)$OHFeSe the resistivity anisotropy increases with decreasing temperature [15] thus suggesting that the intermediate $(Li_{1-x}Fe_x)$OH layers become more insulating. Consequently, instead of expecting that the entire $(Li_{1-x}Fe_x)$OH remains conducting (superconducting), there is a lack of conducting channels between the FeSe layers through the $(Li_{1-x}Fe_x)$OH ones.

There are indications from recent ARPES and STS experiments supporting the validity of the above scenario. STS measurements reveal that the $(Li_{1-x}Fe_x)$OH surface has a metallic behavior when the FeSe layers exhibit superconductivity [18]. The tunneling spectrum has a weak dip at a Fermi level which may point to a superconducting gap opening. We note that the modulation amplitude in STS experiments, $\Delta V = 1$ meV, is comparable to the values of the smallest gap obtained in our studies. ARPES experiments on a similar $(Li_{1-x}Fe_x)$OHFeSe sample show that in addition to the electronlike bands crossing the Fermi level at around the M point, there is a tiny electronlike weight at the Fermi energy near the Γ point, which could be a contribution from the $(Li_{1-x}Fe_x)$OH layers [27]. The presence of such a tiny electron spectral weight might play a crucial role for the proximity effect.

C. Interplay between the superconductivity and magnetism

We want to emphasize that the enhancement of the out-of-plane superfluid density ($\rho_{s,c} \propto \lambda_c^{-2}$) occurs at the same temperature range where the antiferromagnetic order within the $(Li_{1-x}Fe_x)$OHFeSe layers sets in. The theory calculations presented below reveal that carriers within the superconducting FeSe layers are strongly hybridized with the local Fe moments in $(Li_{1-x}Fe_x)$OH. The effect of such hybridization is twofold. First of all, it enhances the superconductivity within the FeSe layers, and, secondly, weak superconductivity with dominant d-wave symmetry can be induced in the insulating $(Li_{1-x}Fe_x)$OH layers. Note that the latter statement is consistent with the $\Delta_d \simeq 1.5$ meV gap obtained from the fit of $\lambda_c^{-2}(T)$ data (see Fig. 11 and Table I).

1. *Theoretical consideration of an interplay between antiferromagnetic and superconducting layers*

To study the interplay between two-dimensional $(Li_{1-x}Fe_x)$OH and FeSe layers, one could consider a two-layer model with model Hamiltonian

$$H = \sum_{\mathbf{k},\sigma} \epsilon_{\mathbf{k}} C^\dagger_{\mathbf{k}\sigma} C_{\mathbf{k}\sigma} + \sum_{\mathbf{k}} \Delta_{\mathbf{k}} (C^\dagger_{\mathbf{k}\uparrow} C^\dagger_{-\mathbf{k}\downarrow} + C_{-\mathbf{k}\downarrow} C_{\mathbf{k}\uparrow}) + J \sum_{<ij>} \mathbf{S}_i \cdot \mathbf{S}_j + K \sum_{i,\sigma\sigma'} \mathbf{S}_i \cdot C^\dagger_{i\sigma} \frac{1}{2} \tau_{\alpha\beta} C_{i\sigma'}. \quad (17)$$

Here the first two terms describe a two-dimensional FeSe layer with the superconducting gap functions $\Delta_{\mathbf{k}}$ for both d_{xz} and d_{yz} orbitals, the third term characterizes the antiferromagnetic (AF) spin exchange interaction among the nearest neighbor local magnetic moments within the two-dimensional insulating $(Li_{1-x}Fe_x)$OH layers, and the last term describes the spin exchange coupling between the local moments and the conduction electrons. If the interlayer coupling is absent ($K = 0$), the local moments of the $(Li_{1-x}Fe_x)$OH layer forms

a paramagnetic phase with strong spin fluctuation at finite temperatures, and the long-range AF order exists *only* at zero temperature. The finite interlayer coupling is certainly helpful for the local magnetic moments to form the AF long-range order above the zero temperature.

In the following, we focus on the paramagnetic phase. The local magnetic moments of spin-1/2 operators have a fermionic representation $\mathbf{S}_i = \frac{1}{2}\sum_{\sigma\sigma'} f^\dagger_{i\sigma}\tau_{\sigma\sigma'}f_{i\sigma'}$ with two local constraints: $\sum_\sigma f^\dagger_{i\sigma}f_{i\sigma} = 1$ and $f_{i\uparrow}f_{i\downarrow} = 0$, where τ is the Pauli matrices. The first constraint restricts any local charge fluctuation, while the second one is imposed by the spin SU(2) symmetry. From the heavy fermion systems it is well known that there is a characteristic temperature T_K, below which the Kondo spin exchange interaction induces a strong hybridization between the local magnetic moments and the conduction electrons. This is because the Kondo spin exchange can be expressed as

$$\mathbf{S}_i \cdot \mathbf{s}_i = -\tfrac{1}{2}(f^\dagger_{i\uparrow}c_{i\uparrow} + f^\dagger_{i\downarrow}c_{i\downarrow})(c^\dagger_{i\uparrow}f_{i\uparrow} + c^\dagger_{i\downarrow}f_{i\downarrow}), \tag{18}$$

where a hybridization parameter can be introduced as $V = -\langle f^\dagger_{i\uparrow}c_{i\uparrow} + f^\dagger_{i\downarrow}c_{i\downarrow}\rangle$. Meanwhile, the AF Heisenberg superexchange can also be expressed as

$$\begin{aligned}\mathbf{S}_i \cdot \mathbf{S}_j = &-\tfrac{1}{4}(f^\dagger_{i\uparrow}f_{j\uparrow} + f^\dagger_{i\downarrow}f_{j\downarrow})(f^\dagger_{j\uparrow}f_{i\uparrow} + f^\dagger_{j\downarrow}f_{i\downarrow})\\ &-\tfrac{1}{4}(f^\dagger_{i\uparrow}f^\dagger_{j\downarrow} - f^\dagger_{i\downarrow}f^\dagger_{j\uparrow})(f_{j\downarrow}f_{i\uparrow} - f_{j\uparrow}f_{i\downarrow}),\end{aligned} \tag{19}$$

and the hopping and pairing order parameters may be induced: $\chi_{ij} = -\langle f^\dagger_{i\uparrow}f_{j\uparrow} + f^\dagger_{i\downarrow}f_{j\downarrow}\rangle$ and $\Delta_{ij} = -\langle f^\dagger_{i\uparrow}f^\dagger_{j\downarrow} - f^\dagger_{i\downarrow}f^\dagger_{j\uparrow}\rangle$.

When the spinon hopping parameter χ is simply chosen as a uniform parameter, the spinons form a very narrow band with a dispersion $\chi_{\mathbf{k}} = J\chi(\cos k_x + \cos k_y) + \lambda$, where λ is the Lagrangian multiplier to impose the local constraint on average. The local constraint $f_{i\uparrow}f_{i\downarrow} = 0$ excludes the extended s-wave pairing, and the d-wave symmetric pairing dominates and $\Delta_{i,i+e_x} = -\Delta_{i,i+e_y} \equiv \Delta_s$. Then a mean field model Hamiltonian can be obtained

$$\begin{aligned}H_{mf} = &\sum_{\mathbf{k},\sigma}\epsilon_{\mathbf{k}}C^\dagger_{\mathbf{k}\sigma}C_{\mathbf{k}\sigma} + \sum_{\mathbf{k}}\Delta_{\mathbf{k}}(C^\dagger_{\mathbf{k}\uparrow}C^\dagger_{-\mathbf{k}\downarrow} + C_{-\mathbf{k}\downarrow}C_{\mathbf{k}\uparrow})\\ &+\sum_{\mathbf{k}\sigma}\chi_{\mathbf{k}}f^\dagger_{\mathbf{k}\sigma}f_{\mathbf{k}\sigma} + \sum_{\mathbf{k}}\Delta_{s,\mathbf{k}}(f^\dagger_{\mathbf{k}\uparrow}f^\dagger_{-\mathbf{k}\downarrow} + f_{-\mathbf{k}\downarrow}f_{\mathbf{k}\uparrow})\\ &+\frac{KV}{2}\sum_{\mathbf{k}\sigma}(c^\dagger_{\mathbf{k}\sigma}f_{\mathbf{k}\sigma} + f^\dagger_{\mathbf{k}\sigma}c_{\mathbf{k}\sigma}) + \text{const},\end{aligned} \tag{20}$$

where $\Delta_{s,\mathbf{k}} \equiv \frac{J\Delta_s}{2}(\cos k_x - \cos k_y)$. Exact diagonalization gives rise to the quasiparticle spectrum, and the mean field order parameters V, Δ_s, and the Lagrangian multiplier λ can be obtained by solving the saddle point equations. Thus the superconducting electrons in the FeSe layer mix with the local moments via the strong hybridization so that the superconductivity of FeSe layer gets enhanced. More importantly, a weak superconductivity with dominate d-wave symmetry can be induced in the insulating $(Li_{1-x}Fe_x)OH$ layer.

V. CONCLUSIONS

In conclusion, the magnetic and superconducting properties of $(Li_{0.84}Fe_{0.16})OHFe_{0.98}Se$ single crystal were studied by means of muon-spin rotation technique. The zero-field and field-shift μSR experiments confirm the homogeneity of the sample and the antiferromagnetic ordering within the $(Li_{0.84}Fe_{0.16})OH$ layers below $T_m \simeq 10$ K. The temperature dependences of the in-plane ($\rho_{s,ab} \propto \lambda^{-2}_{ab}$) and the out-of-plane ($\rho_{s,c} \propto \lambda^{-2}_c$) components of the superfluid density were measured in transverse field μSR experiments. $\lambda^{-2}_{ab}(T)$ was found to be consistent with gap opening within the superconducting FeSe planes, and it is well described within either the single s-wave gap ($\Delta_s = 10.5$ meV) or two s-wave gaps ($\Delta_{s,1} = 15$ meV and $\Delta_{s,2} = 9$ meV) scenario in agreement with the results of ARPES [17] and STS [18] experiments, respectively. The opening of an additional small superconducting gap of unknown symmetry ($\simeq$1.05 meV and 1.5 meV in a case of s- and d-wave symmetry, respectively) was detected from $\lambda^{-2}_c(T)$. This gap, most probably, opens within the insulating $(Li_{1-x}Fe_x)OH$ layers and appears to be induced by the proximity to the superconducting FeSe layers. The strong enhancement of the out-of-plane superfluid density $\rho_{s,c} \propto \lambda^{-2}_c$ occurs at the same temperatures where the magnetism sets in. The question of whether or not the superconductivity and antireferromagnetism within the intermediate $(Li_{1-x}Fe_x)OH$ layers relate to each other requires further studies.

ACKNOWLEDGMENTS

This work was performed at the SμS Paul Scherrer Institute (PSI, Switzerland). The work of H.Z., X.D., and Z.Z. was supported by "Strategic Priority Research Program (B)" of the Chinese Academy of Sciences (Grant No. XDB07020100) and Natural Science Foundation of China (Projects No. 11574370 and No. 11274358). The work of Z.G. was supported by the Swiss National Science Foundation (SNF-Grant No. 290 200021-149486).

[1] S. Margadonna, Y. Takabayashi, Y. Ohishi, Y. Mizuguchi, Y. Takano, T. Kagayama, T. Nakagawa, M. Takata, and K. Prassides, Phys. Rev. B **80**, 064506 (2009).

[2] J. Guo, S. Jin, G. Wang, S. Wang, K. Zhu, T. Zhou, M. He, and X. Chen, Phys. Rev. B **82**, 180520(R) (2010).

[3] A. Krzton-Maziopa, Z. Shermadini, E. Pomjakushina, V. Pomjakushin, M. Bendele, A. Amato, R. Khasanov, H. Luetkens, and K. Conder, J. Phys.: Condens. Matter **23**, 052203 (2011).

[4] A. F. Wang, J. J. Ying, Y. J. Yan, R. H. Liu, X. G. Luo, Z. Y. Li, X. F. Wang, M. Zhang, G. J. Ye, P. Cheng, Z. J. Xiang, and X. H. Chen, Phys. Rev. B **83**, 060512(R) (2011).

[5] Q.-Y. Wang, Z. Li, W.-H. Zhang, Z.-C. Zhang, J.-S. Zhang, W. Li, H. Ding, Y.-B. Ou, P. Deng, K. Chang *et al.*, Chin. Phys. Lett. **29**, 037402 (2012).

[6] J.-F. Ge, Z.-L. Liu, C. Liu, C.-L. Gao, D. Qian, Q.-K. Xue, Y. Liuand, and J.-F. Jia, Nat. Mater. **14**, 285 (2015).

[7] T. P. Ying, X. L. Chen, G. Wang, S. F. Jin, T. T. Zhou, X. F. Lai, H. Zhang, and W. Y. Wang, Sci. Rep. **2**, 426 (2012).

[8] M. Burrard-Lucas, D. G. Free, S. J. Sedlmaier, J. D. Wright, S. J. Cassidy, Y. Hara, A. J. Corkett, T. Lancaster, P. J. Baker, S. J. Blundell *et al.*, Nat. Mater. **12**, 15 (2012).

[9] A. Krzton-Maziopa, E. Pomjakushina, V. Y. Pomjakushin, F. von Rohr, A. Schilling, and K. Conder, J. Phys.: Condens. Matter **24**, 382202 (2012).

[10] S. Hosono, T. Noji, T. Hatakeda, T. Kawamata, M. Kato, and Y. Koike, J. Phys. Soc. Jpn. **83**, 113704 (2014).

[11] X. F. Lu, N. Z. Wang, H. Wu, Y. P. Wu, D. Zhao, X. Z. Zeng, X. G. Luo, T. Wu, W. Bao, G. H. Zhang, F. Q. Huang, Q. Z. Huang, and X. H. Chen, Nat. Mater. **14**, 325 (2014).

[12] U. Pachmayr, F. Nitsche, H. Luetkens, S. Kamusella, F. Brueckner, R. Sarkar, H.-H. Klauss, and D. Johrendt, Angew. Chem. Int. Ed. **54**, 293 (2015).

[13] H. Sun, D. N. Woodruff, S. J. Cassidy, G. M. Allcroft, S. J. Sedlmaier, A. L. Thompson, P. A. Bingham, S. D. Forder, S. Cartenet, N. Mary, S. Ramos, F. R. Foronda, B. H. Williams, X. Li, S. J. Blundell, and S. J. Clarke, Inorg. Chem. **54**, 1958 (2015).

[14] X. Dong, H. Zhou, H. Yang, J. Yuan, K. Jin, F. Zhou, D. Yuan, L. Wei, J. Li, X. Wang, G. Zhang, and Z. Zhao, J. Am. Chem. Soc. **137**, 66 (2015).

[15] X. Dong, K. Jin, D. Yuan, H. Zhou, J. Yuan, Y. Huang, W. Hua, J. Sun, P. Zheng, W. Hu, Y. Mao, M. Ma, G. Zhang, F. Zhou, and Z. Zhao, Phys. Rev. B **92**, 064515 (2015).

[16] A.-M. Zhang, T.-L. Xia, K. Liu, W. Tong, Z.-R. Yang, and Q.-M. Zhang, Sci. Rep. **3**, 1216 (2013).

[17] X. H. Niu, R. Peng, H. C. Xu, Y. J. Yan, J. Jiang, D. F. Xu, T. L. Yu, Q. Song, Z. C. Huang, Y. X. Wang, B. P. Xie, X. F. Lu, N. Z. Wang, X. H. Chen, Z. Sun, and D. L. Feng, Phys. Rev. B **92**, 060504(R) (2015).

[18] Y. J. Yan, W. H. Zhang, M. Q. Ren, X. Liu, X. F. Lu, N. Z. Wang, X. H. Niu, Q. Fan, J. Miao, R. Tao, B. P. Xie, X. H. Chen, T. Zhang, and D. L. Feng, arXiv:1507.02577.

[19] J. E. Sonier, J. H. Brewer, and R. F. Kiefl, Rev. Mod. Phys. **72**, 769 (2000).

[20] A. Suter, internal PSI report (unpublished).

[21] A. Yaouanc and P. Dalmas de Réotier, *Muon Spin Rotation, Relaxation and Resonance* (Oxford University Press, Oxford, 2011).

[22] E. H. Brandt, Phys. Rev. B **37**, 2349(R) (1988).

[23] S. L. Thiemann, Z. Radović, and V. G. Kogan, Phys. Rev. B **39**, 11406 (1989).

[24] W. Chen, C. Zeng, E. Kaxiras, and Z. Zhang, Phys. Rev. B **93**, 064517 (2016).

[25] M. Bendele, A. Ichsanow, Yu. Pashkevich, L. Keller, Th. Strässle, A. Gusev, E. Pomjakushina, K. Conder, R. Khasanov, and H. Keller, Phys. Rev. B **85**, 064517 (2012).

[26] J. E. Sonier, R. F. Kiefl, J. H. Brewer, D. A. Bonn, J. F. Carolan, K. H. Chow, P. Dosanjh, W. N. Hardy, R. Liang, W. A. MacFarlane, P. Mendels, G. D. Morris, T. M. Riseman, and J. W. Schneider, Phys. Rev. Lett. **72**, 744 (1994).

[27] L. Zhao, A. Liang, D. Yuan, Y. Hu, D. Liu, J. Huang, S. He, B. Shen, Y. Xu, X. Liu, L. Yu, G. Liu, H. Zhou, Y. Huang, X. Dong, F. Zhou, Z. Zhao, C. Chen, Z. Xu, and X. J. Zhou, Nat. Commun. **7**, 10608 (2016).

[28] Z. Du, X. Yang, H. Lin, D. Fang, G. Du, J. Xing, H. Yang, X. Zhu, and H.-H. Wen, Nat. Commun. **7**, 10565 (2016).

[29] M. Tinkham, *Introduction to Superconductivity* (Krieger Publishing Company, Malabar, Florida, 1975).

[30] R. Khasanov, A. Shengelaya, A. Maisuradze, F. La Mattina, A. Bussmann-Holder, H. Keller, and K. A. Müller, Phys. Rev. Lett. **98**, 057007 (2007).

[31] A. Carrington and F. Manzano, Physica C **385**, 205 (2003).

[32] Y. Zhang, J. J. Lee, R. G. Moore, W. Li, M. Yi, M. Hashimoto, D. H. Lu, T. P. Devereaux, D.-H. Lee, and Z.-X. Shen, arXiv:1512.06322.

[33] R. Khasanov, A. Maisuradze, H. Maeter, A. Kwadrin, H. Luetkens, A. Amato, W. Schnelle, H. Rosner, A. Leithe-Jasper, and H.-H. Klauss, Phys. Rev. Lett. **103**, 067010 (2009).

[34] M. Bendele, S. Weyeneth, R. Puzniak, A. Maisuradze, E. Pomjakushina, K. Conder, V. Pomjakushin, H. Luetkens, S. Katrych, A. Wisniewski, R. Khasanov, and H. Keller, Phys. Rev. B **81**, 224520 (2010).

[35] Y. J. Song, J. S. Ghim, J. H. Yoon, K. J. Lee, M. H. Jung, H.-S. Ji, J. H. Shim, and Y. S. Kwon, Europhys. Lett. **94**, 57008 (2011).

[36] T. Kondo, R. Khasanov, J. Karpinski, S. M. Kazakov, N. D. Zhigadlo, Z. Bukowski, M. Shi, A. Bendounan, Y. Sassa, J. Chang, S. Pailhés, J. Mesot, J. Schmalian, H. Keller, and A. Kaminski, Phys. Rev. Lett. **105**, 267003 (2010).

[37] R. Khasanov, A. Shengelaya, A. Bussmann-Holder, J. Karpinski, H. Keller, and K. A. Müler, J. Supercond. Novel Magn. **21**, 81 (2008).